Title
In situ nanobeam electron diffraction strain mapping of planar slip in stainless steel

Authors
Pekin, Thomas C
Gammer, Christoph
Ciston, Jim
et al.

Publication Date
2018-03-01

DOI
10.1016/j.scriptamat.2017.11.005

Peer reviewed

Scripta Materialia 146 (2018) 87–90

Contents lists available at ScienceDirect

Scripta Materialia

journal homepage: www.elsevier.com/locate/scriptamat

Regular article

In situ nanobeam electron diffraction strain mapping of planar slip in stainless steel

Thomas C. Pekin[a,b,*], Christoph Gammer[c], Jim Ciston[b], Colin Ophus[b], Andrew M. Minor[a,b,*]

[a] Department of Materials Science and Engineering, University of California, Berkeley, Berkeley 94720, USA
[b] National Center for Electron Microscopy, Molecular Foundry, Lawrence Berkeley National Laboratory, Berkeley 94720, USA
[c] Erich Schmid Institute of Materials Science, Austrian Academy of Sciences, Jahnstrasse 12, Leoben 8700, Austria

ARTICLE INFO

Article history:
Received 7 September 2017
Received in revised form 3 November 2017
Accepted 4 November 2017
Available online 20 November 2017

Keywords:
Nanobeam electron diffraction
Strain measurement
Scanning/transmission electron microscopy
Planar slip

ABSTRACT

Nanobeam electron diffraction strain mapping has been used to measure the strain evolution in stainless steel under in situ deformation. As the amount of deformation increases, the leading dislocation of a planar slip band leaves behind a residual strain in the form of a small lattice expansion. Dislocation analysis confirmed that the dislocations involved were < 011 > type. While the characteristic residual strain of planar slip has often been observed, it has never before been directly measured. Our results provide a view into the dynamic mechanisms of planar slip, and showcase the possibilities of multidimensional in situ imaging.

Published by Elsevier Ltd.

The deformation of crystalline materials is highly dependent on defects and their response to applied stress [1,2]. Understanding the motion and dynamic response of these defects, as well as their interactions with each other, is key to future alloy development. A new tool for quantifiably probing these interactions over a large area is scanning nanobeam electron diffraction (NBED). NBED [3–7] is a scanning transmission electron microscopy (STEM) technique that allows for the quantification of strain fields around features of interest at the level of single nanometers. This method, which utilizes a semi-converged electron beam, is faster than methods utilizing electron beam precession [7–9], and can acquire a larger field of view when compared to methods requiring atomic resolution [6,9,10]. Additionally, while NBED requires a sample close to a zone axis, it is relatively robust to imperfect sample tilt, which is all but guaranteed during an in situ deformation experiment [6]. This combination of speed, robustness to sample orientation [11], and increased field of view has allowed for the development of in situ strain mapping, in which the sample is mechanically deformed while successive strain maps are acquired [12]. While traditional TEM based in situ mechanical testing has been a useful technique in understanding the mechanisms of deformation [13,14], by combining nanoscale deformation with simultaneous strain mapping, we now acquire quantitative data on the local strain field evolution and its relationship with dislocation motion.

It is generally known that the dislocation slip character can be classified in one of two ways [15]. Typically, dislocations either move in three dimensions via wavy slip, or in two-dimensional oriented ensembles known as planar slip [16]. There is a wide body of both experimental and theoretical literature that has shown that the dislocation slip character has a large effect on the resulting mechanical properties of the material, including fracture behavior, fatigue resistance, and stress corrosion cracking [17–24]. In close packed materials (both face-centered cubic (FCC), and hexagonal (HCP)), the presence of short range order (SRO) has been found to be the main factor leading to planar slip [16,25,26].

Planar slip features can be readily observed in lightly deformed stainless steels, as shown in Fig. 1. Fig. 1a is a TEM bright field micrograph of a single instance of planar slip showing multiple dislocations. Fig. 1b is an ADF STEM image showing the long range and regular orientation of these defects.

In alloys containing SRO, planar slip begins when the leading dislocation moves through the matrix, and as it moves, shifts thelattice by a Burgers vector, **b**. This is thought to lead to the local destruction of the SRO, as the locally ordered atoms are shifted out of their energetically favorable positions into a more disordered state. The result of this shift is glide plane softening, which allows further

* Corresponding authors at: Department of Materials Science and Engineering, University of California, Berkeley, Berkeley 94720, USA.
E-mail addresses: tcpekin@berkeley.edu (T.C. Pekin), aminor@berkeley.edu (A.M. Minor).

https://doi.org/10.1016/j.scriptamat.2017.11.005
1359-6462/Published by Elsevier Ltd.

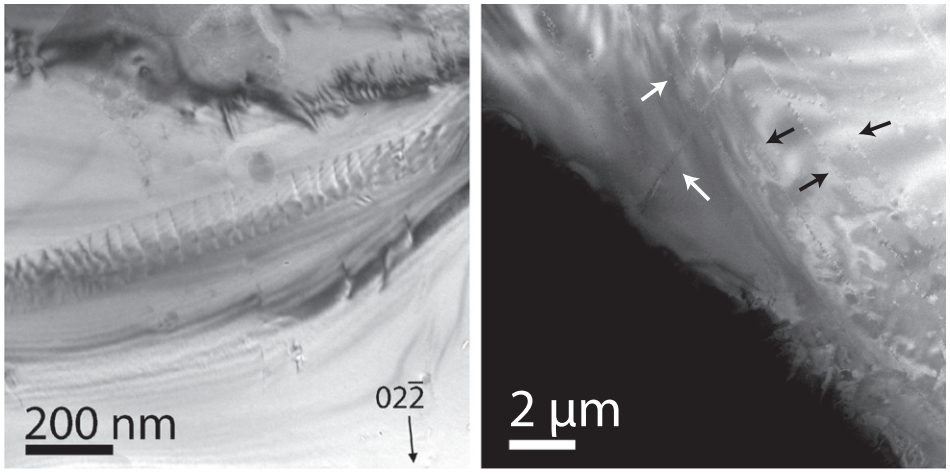

Fig. 1. a) A bright field TEM image of a single instance of planar slip in 321 stainless steel. Note the orderly array of dislocations. b) An ADF STEM image of the same alloy at a lower magnification. Multiple large arrays of planar slip can be seen oriented along specific crystalline directions. Arrows highlight the location of a few of the more prominent examples.

dislocations to move more easily if they follow the first, thereby forming characteristic planar slip bands [16,26]. These highly local, heavily disordered regions then have a deleterious effect on macroscopic mechanical properties due to the resulting stress concentrations as opposed to alloys with more homogeneous wavy slip.

In this experiment, a AISI 321 FCC austenitic stainless steel was pulled in tension in situ in a TEM using a Gatan 654 straining holder. To accurately determine composition, samples were sent to Luvak Inc. for analysis. To determine the majority of the elements in the foil, direct current plasma emission spectroscopy was used [27]. Inert gas fusion was used determine nitrogen composition [28], and combustion infrared detection was used to determine carbon composition [29]. The composition is shown in Table 1. The as rolled foil was electrical discharge machined (EDM) into 11 mm by 2.5 mm blanks, annealed at 1060 ° C for 30 min to anneal out many of the dislocations, and then jet polished to electron transparency using a solution of 6% perchloric acid, 39% butanol and 55% methanol at −15 ° C and approximately 30 V. The scanning NBED was performed on the TEAM 1 microscope which is double aberration corrected, and the diffraction patterns were acquired using the Gatan K2 IS electron detector at 400 frames per second. The microscope was operated at 300 kV, with a convergence angle of 2.62 mrad and a camera length of 230 mm, resulting in a collection angle of 32–160 mrad. Eight loading steps were applied. As the Gatan 654 holder does not measure load or accurate displacement, the tensile bar was elongated until dislocation motion commenced. Loading was then paused and a 100 by 100 pixel NBED map with a 2.2 nm step size was acquired. At 400 frames per second, each map took 25 s. Post-deformation ex situ dislocation characterization was performed on the same sample, but in a different region as the in situ region was destroyed during the in situ test. The dislocation characterization was performed on a JEOL 3010 TEM at 300 kV, and the dislocations were found to be [011] type perfect dislocations, as were all dislocations analyzed in similarly prepared samples. The strain mapping analysis was processed using MATLAB, using the hybrid method detailed in [11]. The reference lattice chosen was the mean diffraction pattern for each frame, resulting in a map showing the deviation from the mean strain at each discretely applied load. Post-processing included cropping to remove exceptionally noisy areas and smoothing. The smoothing was applied using the VBM4D MATLAB package [30], which is optimized for video data.

Table 1
The alloy composition as tested.

Element	Fe	Cr	Ni	Mn	Si	Ti	C	N
wt%	Bal.	17.74	9.25	1.71	0.53	0.33	0.031	0.018

The results (full video available online in Supplementary materials) can be seen in Fig. 2. Three discrete time-steps are shown, with a, e and i showing the annular dark field (ADF) images acquired simultaneously at each step. Several features can be seen in the ADF images, including a strong bend contour, several dislocations, and a circular precipitate used as a reference for aligning the video frames. However, only one dislocation is caught moving in the field of view from left to right. This is the top dislocation in the image, and it moves a small amount from a to e, while in i it has fully propagated across the field of view. The white arrows denote the location of the leading dislocation. As the dislocation moves, it leaves behind a region of increased contrast in the ADF images. This region of higher contrast matches the band directly beneath it, which was observed previously in the same experiment to be another instance of planar slip in parallel with the moving dislocation shown here.

Strain maps are also shown in Fig. 2. The maps are rather complex as we are measuring the transient strains around multiple dislocations and precipitates in situ. Examining the evolution of strain with respect to deformation, there are some very interesting observations. As the leading dislocation of planar slip moves from left to right, the strain in the 200 direction increases behind it. However, in the perpendicular 02$\bar{2}$ direction, strain remains constant, showing clear directionality when it comes to the lattice expansion. The evolution during loading of the lattice expansion ($(\epsilon_{200} + \epsilon_{02\bar{2}})/2$) is shown in Fig. 2d, h, and l. Color coded line profiles (10 pixel integration width) from between the arrows in the expansion maps are shown in subpanel n. While the consistent large dips in the line profiles are due to deleterious effects of sample bending during strain mapping analysis, the profiles reveal that in the second loading step, there is a small lattice expansion as the dislocation moves from left to right, and then at the final loading step, the entire profile is shifted up roughly 0.15%. This corresponds to lattice expansion of 0.3%. This small, directional lattice expansion is not unexpected. In fact, when observing planar slip with standard TEM techniques, it is somewhat characteristic of planar slip to leave behind weak fringing. While we do not see the fringing in our ADF images during strain mapping due to the zone axis imaging condition, we can see them in Fig. 3, which is a representative ex situ 2-beam TEM image of a similar planar slip band from an intact region after releasing the tensile load for deformation.

The weak fringing observed in Fig. 3 is another manifestation of the residual displacement or strain that was observed behind the first

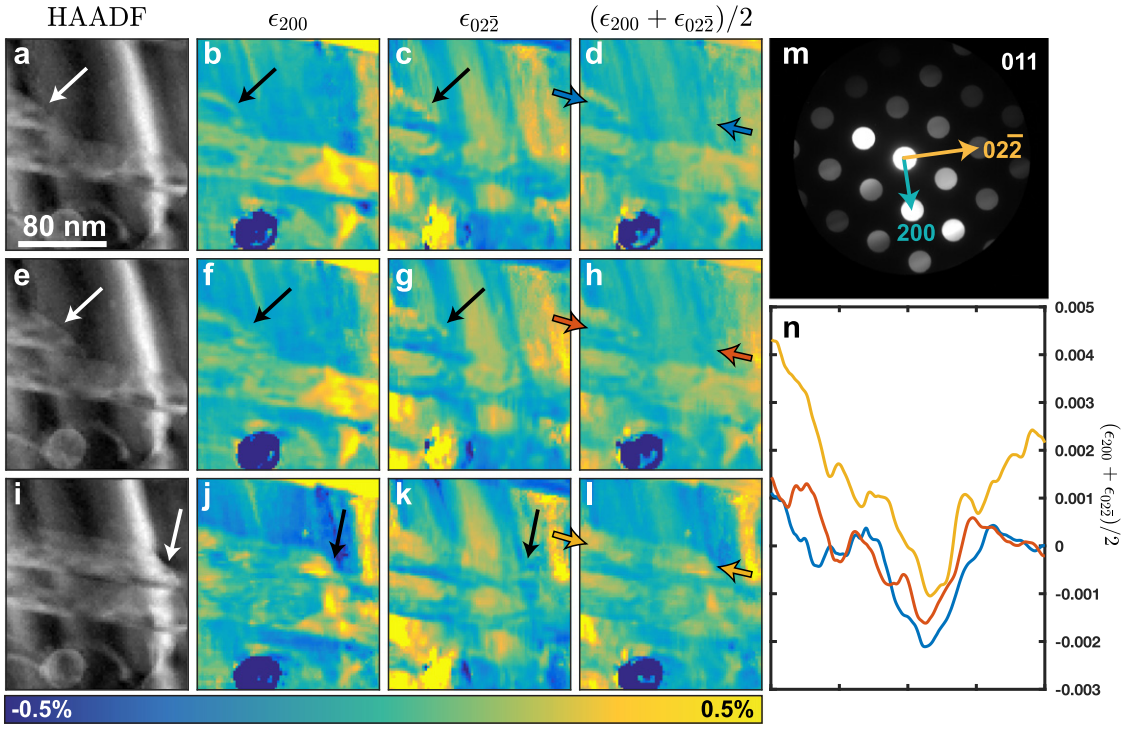

Fig. 2. a, e, i) ADF images obtained at increasing levels of deformation. The white arrows denote the leading dislocation location. b, f, j) Strain mapped in the 200 and c, g, k) $02\bar{2}$ directions. The black arrows correspond to the leading dislocation location. d, h, l) Lattice expansion behind the leading dislocation of planar slip. m) Correctly oriented mean diffraction pattern showing the crystallographic directions chosen for strain axes. n) 10 pixel integrated line profiles of the area between the color coded arrows in d, h, and l. The horizontal axis corresponds to position from left to right between the arrows, and the vertical axis corresponds to lattice expansion. A lattice expansion can be seen behind the planar slip front.

dislocation measured in Fig. 2. This fringing can be correlated to the destruction of SRO [31] by a dislocation passing through the matrix, and leaving behind some residual lattice displacement. In previous studies, by using quantitative image matching with simulations, the estimated displacement that results in residual fringing was found

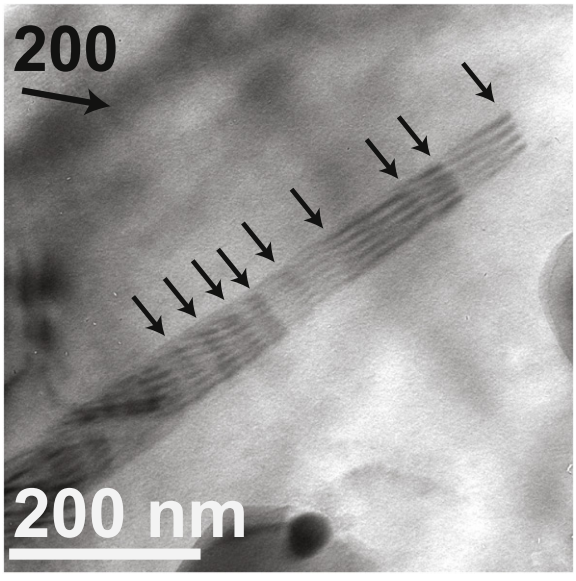

Fig. 3. Representative TEM image of planar slip in 321 stainless steel. The arrows denote the locations of perfect $< 011 >$ dislocations, and the fringe pattern perpendicular to the arrows/dislocations is indicative of a residual displacement, or strain, in the planar slip plane.

to be between $1/150$ and $1/200 < 111 >$ in a FCC Cu-Al alloy [32], $-1/50 < 110 >$ in a FCC Pd-Ce alloy, and between $1/104\left[11\bar{2}0\right]$ and $1/145\left[11\bar{2}0\right]$ in an HCP Ti-Al alloy [31]. Particularly for the FCC Cu-Al alloy, the displacement when converted to strain (displacement/$\sqrt{3}$) is in the range of 0.28–0.38%, which is very similar to the values measured using our NBED technique. While the fringing in the two previously studied FCC alloys is attributed to atomic size differences and unfavorable atomic positions after the destruction of SRO, in the Ti-Al system this cannot be the case due to relatively similar atomic radii, and instead is hypothesized to be caused by unfavorable nearest neighbor interactions [31,33]. It is important to note that the sample studied here has a much more complex chemistry than the previously studied materials, and thus we must be cautious about a direct comparison between lattice expansion of the Cu-Al system and ours. The stainless steel contains multiple substitutional elements with roughly similar atomic size and weights, as well as several light interstitial elements, and thus making strong conclusions about the exact mechanisms behind this observed strain difficult. However, we believe the general mechanism should be the same as the previous studies, in which the destruction of SRO and a new, unfavorable atomic configuration causes a local lattice expansion. Hindering our ability to confirm this hypothesis is the difficulty of observing or measuring SRO in the alloy studied, in which all the substitutional species scatter equivalently in an electron microscope, and in which the primary interstitial elements (C and N) cannot be directly imaged.

More importantly, we showcase in this paper a technique in which a lattice expansion is directly measured during in situ deformation via a nanobeam electron diffraction experiment. This is important for two reasons. First, it shows that it is possible to record the dynamic processes that occur during the deformation of a

material and extract quantitative data from a previously qualitative technique. This has relevancy for in situ deformation as shown here, but it should be able to be extended to many other in situ techniques, including temperature control and electrical biasing. Second, particular to this experiment, a direct measurement of the expansion due to planar slip can be made without resorting to quantitative image matching at multiple zone axes. Using the in situ scanning NBED technique, we have for the first time directly measured this expansion in a commercially relevant stainless steel, and shown that it is due to dislocation motion in situ, rather than inferring it from ex situ measurements.

The authors acknowledge support by the Director, Office of Science, Office of Basic Energy Sciences, Materials Sciences and Engineering Division, of the U.S. Department of Energy under Contract No. DE-AC02-05CH11231 under the Mechanical Behavior of Materials program. CG acknowledges support by the Austrian Science Fund (FWF):[J3397]. Work at the Molecular Foundry was supported by the Office of Science, Office of Basic Energy Sciences, of the U.S. Department of Energy under Contract No. DE-AC02-05CH11231. JC acknowledges additional support from the US Department of Energy Early Career Research Program. The authors also thank Profs. Daryl Chrzan, Mark Asta, and Michael Mills as well as student Max Poschmann for insightful discussions.

Supplementary data to this article can be found online at https://doi.org/10.1016/j.scriptamat.2017.11.005.

References

[1] J.P. Hirth, J. Lothe, Theory of Dislocations, John Wiley & Sons. 1982.
[2] G.I. Taylor, Proc. R. Soc. London, Ser. A, Containing Pap. Math. and Phys. Character 145 (855) (1934) 362–387.
[3] A. Béché, J. Rouvière, L. Clément, J. Hartmann, Appl. Phys. Lett. 95 (2009) 123114.
[4] D. Cooper, A. Béché, J.M. Hartmann, V. Carron, J.-L. Rouvière, Semicond. Sci. Technol. 25 (2010) 095012.
[5] C. Gammer, V.B. Ozdol, C.H. Liebscher, A.M. Minor, Ultramicroscopy 155 (2015) 1–10.
[6] V. Ozdol, C. Gammer, X. Jin, P. Ercius, C. Ophus, J. Ciston, A. Minor, Appl. Phys. Lett. 106 (2015) 253107.
[7] K. Müller, H. Ryll, I. Ordavo, S. Ihle, L. Strüder, K. Volz, J. Zweck, H. Soltau, A. Rosenauer, Appl. Phys. Lett. 101 (2012) 212110.
[8] K. Müller, A. Rosenauer, M. Schowalter, J. Zweck, R. Fritz, K. Volz, Microsc. Microanal. 18 (2012) 995–1009.
[9] D. Cooper, T. Denneulin, N. Bernier, A. Béché, J.-L. Rouvière, Micron 80 (2016) 145–165.
[10] M.J. Hÿtch, L. Potez, Philos. Mag. A 76 (1997) 1119–1138.
[11] T.C. Pekin, C. Gammer, J. Ciston, A.M. Minor, C. Ophus, Ultramicroscopy 176 (2017) 170–176.
[12] C. Gammer, J. Kacher, C. Czarnik, O. Warren, J. Ciston, A. Minor, Appl. Phys. Lett. 109 (2016) 081906.
[13] Z.W. Shan, R.K. Mishra, S.S. Asif, O.L. Warren, A.M. Minor, Nat. Mater. 7 (2008) 115.
[14] Z.J. Wang, Q.J. Li, Z.W. Shan, J. Li, J. Sun, E. Ma, Appl. Phys. Lett. 100 (2012) 2010–2013.
[15] J.C. Williams, A.W. Thompson, R.G. Baggerly, Scr. Metall. 8 (1974) 625–630.
[16] V. Gerold, H. Karnthaler, Acta Metall. 37 (1989) 2177–2183.
[17] T. Johnston, R. Davies, N. Stoloff, Philos. Mag. 12 (1965) 305–317.
[18] A. McEvily, T. Johnston, Int. J. Fract. Mech. 3 (1967) 45–74.
[19] C. Feltner, C. Laird, Acta Metall. 15 (1967) 1621–1632.
[20] C. Feltner, P. Beardmore, Strengthening mechanisms in fatigue, Achievement of High Fatigue Resistance in Metals and Alloys, ASTM International. 1970, pp. 77–112.
[21] D. Koss, K. Chan, Acta Metall. 28 (1980) 1245–1252.
[22] K. Tanaka, T. Mura, Acta Metall. 32 (1984) 1731–1740.
[23] P. Swann, Corrosion 19 (1963) 102t–114t.
[24] J.-O. Nilsson, Scr. Metall. 17 (1983) 593–596.
[25] T. Neeraj, M. Mills, Mater. Sci. Eng. A 319 (2001) 415–419.
[26] K. Wolf, H.-J. Gudladt, H. Calderon, G. Kostorz, Acta Metall. Mater. 42 (1994) 3759–3765.
[27] ASTM, Standard Guide for Determination of Various Elements by Direct Current Plasma Atomic Emission Spectrometry, ASTM E1097-12, ASTM International, West Conshohocken, PA, 2017,
[28] ASTM, Standard Test Methods for Determination of Carbon, Sulfur, Nitrogen, and Oxygen in Steel, Iron, Nickel, and Cobalt Alloys by Various Combustion and Fusion Techniques, ASTM E1019-11, ASTM International, West Conshohocken, PA, 2011,
[29] ASTM, Standard Test Methods for Determination of Carbon, Sulfur, Nitrogen, and Oxygen in Steel, Iron, Nickel, and Cobalt Alloys by Various Combustion and Fusion Techniques, ASTM E1019-08, ASTM International, West Conshohocken, PA, 2008,
[30] M. Maggioni, G. Boracchi, A. Foi, K. Egiazarian, IEEE Trans. Image Process. 21 (2012) 3952–3966.
[31] T. Neeraj, M. Mills, Philos. Mag. A 82 (2002) 779–802.
[32] L. Clarebrough, Phys. Status Solidi (a) 18 (1973) 427–438.
[33] F. Grégori, P. Veyssière, Philos. Mag. A 79 (1999) 403–421.